Analyst

Microfluidic Pressure in Paper (μPiP): Rapid Prototyping and Low-Cost Liquid Handling for On-Chip Diagnostics

Journal:	*Analyst*
Manuscript ID	AN-ART-09-2021-001676.R1
Article Type:	Paper
Date Submitted by the Author:	11-Dec-2021

Complete List of Authors:	Islam, Md. Nazibul; Texas A and M University College Station, Chemical Engineering Yost, Jarad; Texas A&M University, Chemical Engineering Gagnon, Zachary; Texas A and M University College Station, Chemical Engineering

SCHOLARONE™
Manuscripts

Microfluidic Pressure in Paper (µPiP): Rapid Prototyping and Low-Cost Liquid Handling for On-Chip Diagnostics

Md. Nazibul Islam[1], Jarad W. Yost[1], Zachary R. Gagnon[1]*

[1]Artie McFerrin Department of Chemical Engineering, Texas A&M University

*Corresponding author: zgagnon@tamu.edu

Abstract

Paper-based microfluidics was initially developed for use in ultra-low-cost diagnostics powered passively by liquid wicking. However, there is significant untapped potential in using paper to internally guide porous microfluidic flows using externally applied pressure gradients. Here, we present a new technique for fabricating and utilizing low-cost polymer-laminated paper-based microfluidic devices using external pressure. Known as microfluidic pressure in paper (µPiP), devices fabricated by this technique are capable of sustaining a pressure gradient for use in precise liquid handling and manipulation applications similarly to conventional microfluidic open-channel designs, but instead where fluid is driven directly through the porous paper structure. µPiP devices can be both rapidly prototyped or scalably manufactured and deployed at commercial scale with minimal time, equipment and training requirements. We present an analysis of continuous pressure-driven flow in porous paper-based microfluidic channels and demonstrate broad applicability of this method in performing a variety of different liquid handling applications, including measuring red blood cell deformability and performing continuous free-flow DNA electrophoresis. This new platform offers a budget-friendly method for performing microfluidic operations for both academic prototyping and large-scale commercial device production.

1. Introduction

Microfluidic engineering and microfabrication technology go hand-in-hand. In the last two decades there has been an explosion of new microfluidic devices made feasible largely in part by the invention of soft lithography. Today, soft lithography microfluidics receives significant attention from both academia and industry, and researchers report thousands of new prototype devices each year for use in a broad range of environmental, pharmaceutical, and biomedical engineering applications [1-3]. While the global microfluidics market size is expected to reach USD $31.6 billion by 2027 [4], very few of these microfluidic devices are successfully translated to commercial products [3]. One reason for low market penetration is the absence of low-cost high throughput manufacturing technique that can bridge the gap between budget-friendly academic prototyping efforts and often high budget commercial scalability requirements conventionally satisfied by modern industrial manufacturing techniques [1-3, 5]. In academia, soft lithography has been a predominant choice for the fabrication of microfluidic devices [1, 3, 5]. While effective in prototyping, this method is labor-intensive, requires a cleanroom facility and is not easily scalable. In contrast, in a commercial setting the largescale manufacturing of microfluidic devices is typically accomplished using injection molding or hot embossing techniques [1, 5]. These methods have significantly higher throughput and are capable of manufacturing thousands of devices per day. However, such manufacturing techniques often require large upfront capital equipment, tooling and development costs. While powerful and mature, these fabrication methods are often financially infeasible for an academic or small commercial start-up interested in commercializing their work and can serve as both financial and technical barriers to translation of microfluidic technology from a single prototype device to the commercial marketplace.

Over the past decade, paper-based microfluidics has gained widespread attention for creating disposable microfluidic devices for ultra-low-cost diagnostics [6-9]. Fluid control is initiated passively; paper is hydrophilic in nature and different techniques such as, photolithography, plasma oxidation, cutting, and wax printing can be used to create and pattern hydrophobic zones within a paper matrix to create no-flux liquid boundaries for directing microfluidic flows. Fluid transport typically takes within the porous paper structure via capillary action [7, 10, 11], which then is the main fluid driving force for lateral flow assays and colorimetric detection devices [6, 8, 12-15].

While passive fluid handling on paper is a significant benefit for many applications, the lack of active fluid control and the resulting variability in capillary transport due to evaporation is a major technical limitation for paper-based microfluidic devices [8]. Such a lack in reproducibility and controllability in real-world environmental conditions have limited paper-based microfluidics from successfully competing with traditional open-channel systems manufactured by injection molded technologies [6, 9]. A range of alternative techniques for the fabrication of microfluidic devices that combine both polymeric sheets and paper channel structures. Much of these efforts use paper to fabricate open channel designs. For example, Glavan et al. reported a pressure driven, open channel microfluidic system that uses a craft cutter to carve micro-channels on the surface of cardstock paper. While this work combines the use of pressure with paper, fluid flow is still driven in an open channel using a traditional style open channel constructed from paper. The paper is chemically treated with alkyl or fluoroalkyl trichlorosilane to render it hydrophobic and the open channel is subsequently closed with a layer of tape [16]. Yi et al., have reported a paper-based fabrication technique where a laser cutter is used to cut open cutout design within a paper matrix. The paper is sandwiched between two glass or PMMA slides and the paper gap is treated to a mixture of cyanoacrylate-based resin to block fluid flow out into the paper sidewalls and create a paper-defined open channel design [17]. Shin et al., have reported a hybrid paper-plastic fabrication that utilizes a combination of capillary and hydrostatic-based Poiseuille flow [18]. Hydrophilic channels were fabricated on paper using a traditional wax printing method and placed atop a film with an identical open channel geometry. The wax printed paper and hollow structure was then sandwiched between cold laminate films. The final device has a top cover, a middle void layer for fluid flow, a paper layer for capillary flow and a bottom cover [18]. Fluid flow is initiated using a combination of hydrostatic pressure to drive flow over the paper surface and capillary wicking to simultaneously wet the bottom paper layer.

Paper devices with capillary flows function without external pumping hardware and offer significant reduction in platform complexity, and hybrid devices with open channel components offer easy-to-prototype inexpensive alternatives to conventional polymer-based open channel fluidic devices. The above hybrid paper-polymer designs expand the features and capabilities that can be performed using paper. However, no existing devices utilize external pressure to drive flow directly and solely through the porous paper microfluidic channels. In this work, we report a novel low-cost method for fabricating pressure-driven paper-based microfluidic devices which use pressure driven flow to drive fluid directly through the porous paper medium. We call this technique “Microfluidic Pressure in Paper” (μPiP). In μPiP, we utilize a CO_2 laser to rapidly cut fluidic channel designs from a sheet of paper. We then confine these paper channels between two thin flexible PDMS membranes. Using a combination of corona plasma treatment and a benchtop thermal press (~5.5 MPa), we confine and irreversibly seal these paper channels within the membranes. This workflow can also be modified and used for other non-silicon base polymer films such as thermoplastics. Using this novel workflow, the final μPiP channels are tightly and precisely laminated and void of any air bubbles or structural deformation. We utilize a constant pressure system to drive fluid through the paper channels in the same way that flows are driven through conventional PDMS-based fluidics and commercial injection molded chips. We first investigate the pressure-driven characteristics of continuous fluid flow through paper channels and show fluidic compatibility with a wide variety of classical microfluidic geometries. We then demonstrate the applicability of μPiP with two liquid handling assays: quantifying red blood cell deformation and continuous electrophoretic concentration of DNA. To the best of our knowledge, this is the first time external pressure has been used to drive microfluidic flows directly through porous paper-based microfluidic channels.

2. Methods

2.1 Device Fabrication

The μPiP fabrication workflow is depicted in Fig. 1. The entire fabrication process, from design to μPiP device, takes less than 10 minutes. The fabrication begins by first cutting a microfluidic channel geometry from a sheet of filter paper (Whatman

Grade 1, 4 etc.) using a CO_2 laser cutter (LS-2440, Boss Laser), however, many low budget K40-style laser cutters and cutting plotters (~$400.00 USD) are also capable of performing this fabrication workflow. Depending on the size of the unit, these laser cutters can precisely and rapidly cut hundreds of paper channels with a dimension as small as 500 µm across large area (~1 m^2) sheets of paper. Each paper channel is then sealed between two thin flexible sheets of polydimethylsiloxane (PDMS). The final stiffness of the µPiP device can be controlled using sheets of different PDMS film thickness. For fluid flow visualization and quantification, channels were laminated within a 0.5 mm PDMS sheet (0.02 inch, McMaster-Carr) as a “top” layer and a 0.12 mm PDMS sheet (0.005 inch, McMaster-Carr) as the “bottom” layer. For RBC deformation analysis and DNA electrophoresis, channels were laminated between two 0.5 mm PDMS sheets. Copper tape electrode (McMaster Carr) and copper wires to connect electrodes to external voltage generator were used for DNA electrophoresis experiments. Fluidic channel inlets/outlets were hole punched on the top PDMS sheet using a 0.75mm biopsy punch (Ted Pella, Inc). The two sheets were then oxidized and irreversibly bonded together using oxygen plasma generated with a handheld tesla coil (Electro-Technic Products, Model BD-20AC). Lastly, the sealed PDMS device was immediately placed into a small bench top heat press (Dulytek DW 400) at a temperature of 95^{o}C for 5 minutes which removed all observable air gaps and bubbles surrounding the paper channel structure.

Pressure driven flow was controlled externally using either a constant pressure source or a constant flow rate source. First, 0.1 mm ID tubing (Cole Palmer) was connected to a small pressurized 5 mL cryovial. A small 1 cm long, 0.64 mm ID stainless steel tube (New England Small Tube) was inserted into the other tubing end and plugged into the biopsy-punched fluidic ports on the top of the PDMS sheet. A low-cost constant pressure system (fabrication cost ~USD $500) [19] was used to pressurize the cryovial and ultimately drive flow fluid through the paper channels. The use of the pressure system for this work allows for the precise variation and control of the external pressure for flow characterization. However, alternative low-cost sources of pressure via miniature vacuum or air pumps are capable of driving flows in µPiP paper channels as the pressures required for the work presented here are less than 4 psig. All experiments except concentration of DNA by electrophoresis were conducted with a constant pressure source. For DNA concentration, however, a syringe pump (Chemyx Fusion 100) was used to deliver a constant and known 5 µL/min flow rate.

2.2 Samples and Reagents

2.2.1 Flow Visualization and Image Analysis

To visualize and quantify pressurized fluid flow through paper, 150 mM methylene blue dye, 800 µM erioglaucine and 1870 µM tartrazine (Sigma-Aldrich) were used. To promote lower cost image acquisition solutions, the images of the flow profiles of pressurized fluid flow and red blood cell deformation were captured using a high-definition cell phone camera (Google Pixel 3a). Captured images were analyzed using ImageJ software (ImageJ 1.47t).

2.2.2 Blood Sample Preparation

RBC deformation experiments were performed using commercially available animal and human blood. No blood samples – animal or human – were collected at Texas A&M University. Bovine, horse, sheep, and goat whole blood in citrate anticoagulant were purchased commercially from a USDA-inspected animal donor facility, Quad five (Materials Bio, Inc.). Single donor human whole blood in CPD was also purchased commercially from an FDA approved facility, ZenBio Inc. All human donors passed required FDA screening and provided informed consent prior to blood collection. Blood experiments were conducted in a BSL-2 certified laboratory approved for use with human blood. The samples were stored at 4^{o}C in a blood bank refrigerator (Jewett). For red blood cell deformation analysis, 1 mL of each whole blood samples were centrifuged at 2000 relative centrifugal force (rcf) for 2 minutes to pellet the RBCs, and the supernatants were pipetted off and replaced with fresh 1X PBS prepared from 10X PBS stock (Quality Biological). This washing procedure was repeated three times and cells were then resuspended into fresh 1X PBS buffer and driven through single paper channels using a syringe pump. For non-deforming control experiments, human RBCs were rendered non-deformable through crosslinking in a 2.5 wt% glutaraldehyde solution in 1X PBS for 30 minutes and washed in the same manner. For each blood sample and μPiP flow experiment the final RBC hematocrit (hct) was held constant at 33% hct.

2.2.3 DNA Electrophoresis

Electrophoresis experiments were performed by adding electrodes to the μPiP devices. Each device consisted of a t-shaped channel paper strip with one inlet and two outlets and a single strip of conductive copper tape to serve as an active electrode. A variable switching DC power supply (TekPower, TP12001X) was used to drop a 100V DC potential across the two electrodes to initiate electrophoresis. The electric field itself was dropped between the copper strip and a corresponding metal syringe needle at the device exit. Prior to electric field application, a channel outlet was temporarily covered with a slab of PDMS. A metal needle was inserted into the PDMS, piercing the paper and serving as a grounding connection point. To induce the electric field for electrophoresis, a 100 V potential was applied across the channel width between the copper tape and the grounding needle for a total of 20 minutes. The current varied from 0.04 to 0.08 mAmp. After 20 minutes, the paper in Outlet 1 and Outlet 2 was extracted for qPCR analysis.

A fluorescently-labelled DNA buffer solution was driven down the channel at a constant flow rate and exposed to the transverse electric field. A stock solution of DNA (88 bp, randomly generated, Integrated DNA Technologies) was made containing 20 mM Bis-Tris (Sigma), 20 mM Tricine (Sigma), 1x SYBR (Lonza), and 50 nM DNA (IDT). SYBR was used to visualize DNA deflection in the ChemiDoc (Bio-Rad Laboratories, Inc). Prior to DNA experiments, the devices were soaked in 3% w/v BSA (Sigma) in diH_2O for forty minutes, followed by washing with diH_2O for 30 minutes. The DNA solution was then flowed through the device and 1 μl samples were collected from the device channel outlets (labeled 1 & 2) for analysis by qPCR using a Bio-Rad CFX96 real-time PCR system.

2.2.4 qPCR

To analyze the degree of DNA concentration due to electrophoresis, quantitative PCR (qPCR) was used to track the shift in cycle quantification (Cq) values, which correspond to a shift in DNA concentration. Collected liquid samples were diluted 1:100 in diH_2O twice, for a final dilution of 1:10,000. The qPCR reaction (10 µl final volume) contained 1x qPCR mix (Bio-Rad), 250 nM forward primer (IDT), 250 nM reverse primer (IDT), and 1:100 diluted DNA sample (final dilution of DNA is 1:100,000). The samples that were analyzed by qPCR were 0V: Outlet 1 & Outlet 2, 100 V: Outlet 1 & Outlet 2, and the original DNA stock, for a total of five samples. Thermal cycler amplifications were cycled between 95ºC for five seconds and 60 ºC for thirty seconds, for forty cycles. After amplification, the qPCR data was analyzed using CFX Maestro software (Bio-Rad).

3. Results

3.1 Pressurized Fluid Flow Through Paper Channels

We now present experiments demonstrating the flow behavior of µPiP channels using external pressure, and how this differs from conventional non-laminated paper-based devices. We fabricated three classic Whiteside's microfluidic "Christmas tree" gradient generators. The fluidic flow field within each device was imaged using deionized water labelled with colored dye. For the non-laminated version of the device, fluid initially wet the paper and flows through by capillary action, however, fluid wicking quickly slowed and ultimate ceased to continue after 60 minutes due to surface evaporation (Fig. 2a). We next tested a device without external pressure, but now we laminated the paper channel using the above described µPiP lamination technique. As shown in Fig. 2b while lamination eliminated surface evaporation and allowed complete wetting of the device, this process required 140 minutes to fully wet the gradient generator channel. Finally, we used pressurized fluid flow to drive fluid into and through the gradient generator (Fig. 2c). The µPiP device fully primed in 15 minutes, approximately 161% faster than the time required to passively wet 50% of the non-laminated gradient generator channel. Further, the flow generated by pressure is continuous and therefore the gradient generator flow profile can be sustained without the flow ceasing. To the best of our knowledge at the time of writing, this is the first reported case of a concentration gradient produced using continuous flow thorough a paper microfluidic device.

With the ability to drive continuous flows through paper, we next quantified the relationship between the applied pressure to a single μPiP channel to that of the observed liquid wicking velocity. In non-laminated paper-based devices fluid flow occurs passively via capillary action, and the Lucas-Washburn equation has been successfully used to model flow through paper by this mechanism [20, 21]. The majority of these paper-based devices are open to the external environment, and flow can therefore be influenced by liquid evaporation. While the Lucas-Washburn equation model does not consider evaporative transport, Liu *et al.* modified the equation to include an evaporative contribution when predicting the fluid wicking length (h_{ev}) through a paper channel [20]:

$$h_{ev} = 2N \cdot e^{-Mt} \int_0^{\sqrt{t}} e^{Mt^2} dt \qquad (1),$$

where, $N = \sqrt{\frac{\sigma \cos(\theta)}{\mu} \frac{K}{\epsilon R}}$ and $M = \frac{2m^*_{ev}}{\rho \varepsilon \delta}$

Here, N is a modified version of Lucas-Washburn equation based on a momentum balance between capillary pressure and viscous stress, and h_o, $\sigma, \theta, \mu, K, \epsilon, R$, and t are the theoretical wicking liquid front height, interfacial tension, viscosity, contact angle, permeability, effective pore size, paper pore radius, and time, respectively. The term, M represents the total evaporation mass, and m^*_{ev}, ρ *and* δ are evaporation rate, density and paper strip thickness, respectively. The terms, N and M are used with Eq. (1) to model the effect of evaporation on wicking height over a time period of t. Because paper channels in μPiP are enclosed in two PDMS membranes, fluid transport by evaporation through PDMS was calculated to be only 1.03% of the rate of evaporation at experimental laboratory conditions (25^{o}C, 35% Relative Humidity). Therefore, we neglected the influence of evaporation, and fluid flow in a pressurized μPiP channel was assumed to be accomplished through a linear combination of capillary wetting and transport in a porous media by a pressure gradient. Combining Darcy's Law with the Lucas-Washburn equation, and neglecting evaporation, the theoretical μPiP liquid penetration height (h_o) as a function of time, t is:

$$h_o = \sqrt{\frac{4\sigma \cos(\theta)}{\mu} \frac{K}{\epsilon R}} \cdot t^{1/2} + \frac{K \Delta P}{\mu L} \cdot t \qquad (2),$$

where the first term in Eq. (2) captures the influence of capillary wetting and the second is the contribution to flow via an applied pressure gradient (ΔP) over a channel length, *L* for a given time, *t*. To evaluate the proposed model with experimental data, available physical parameters of water and Whatman #1 filter paper were used (interfacial tension: 727.1X10^{-4} N/m, contact angle: 80^{o}, viscosity: 9.6075X10^{-4} Pa-sec, density: 997.05 kg/m^3, paper thickness: 0.18 mm and, mean fiber radius: 0.0082 mm). Permeability of paper, *K* for a given pore size, *r*, was calculated using Eq. (3) [20]:

$$K = r^2 \frac{\pi\varepsilon(1-\sqrt{1-\varepsilon})^2}{24(1-\varepsilon)^{1.5}} \qquad (3),$$

Wicking height was tracked in µPiP channels fabricated from Whatman #1 filter paper that was laser cut into strips 2 mm in width and 100 mm in length (Fig. 3). The liquid penetration height for a given pressure drop was measured and then compared to the conventional passively driven non-laminated microfluidic equivalent. Flow was characterized using deionized water labelled with 150 mM methylene blue (Sigma Alrich). Shown in Fig. 3a, under the application of a continuous and fixed externally applied pressure, liquid transport was observed as a moving liquid front advancing down the length of the paper channel. The resulting length of this front was then dynamically measured for different inlet pressures: 0.0 psi (e.g., pure capillary wetting), 0.5 psig, and 1.0 psig. During the flow experiments, high-resolution images were captured every 30 seconds for a period of 300 seconds using a high resolution cellphone camera (Fig. 3b). For pure capillary flow in an open channel (i.e. non-laminated), the effective porosity was calculated using Eq. (1) and determined to be $\epsilon = 0.65$, which is in agreement with previously published data for Whatman #1 filter paper [20, 22]. The paper channels were then encapsulated in PDMS sheets according to the µPiP fabrication workflow and the fluid flow experiment was repeated at a pressure of 0.0 psig. As shown in Fig. 3c, the rate of the moving front in encapsulated channels is reduced approximately 62% when compared to open channels. From Eq. (1), the effective porosity of the laminated µPiP channel was calculated to be 0.25. Therefore, we speculate that the heat press and subsequent hydraulic encapsulation of the paper channels in PDMS sheets likely results in a decreased effective porosity of paper channels and results in a decreased flow.

We next investigated the influence of a pressure gradient on the liquid wetting length for two different non-zero inlet pressures: 0.5 psig and 1.0 psig, and an outlet pressure vented to atmosphere (0.0 psig). As shown in Fig. 3b, there is an observed increase rate of wicking height with applied pressure. Further, unlike the two purely capillary flow experiments in which the observed liquid velocity decreases with increasing transport time, the pressurized fluid velocity (wicking height length per unit time) remains approximately constant (constant slope) with transport time over the period of 300 seconds.

We now demonstrate the applicability and usefulness of μPiP through presenting two applications. The first leverage the porous nature of the paper channel to characterize the deformability of human red blood cells. The second demonstrates a continuous flow device for concentrating by electrophoresis.

3.2 RBC Deformability Test

μPiP enables the design of liquid assays which leverage the porous nature of the paper material. We now demonstrate the ability to use μPiP with porous paper and complex fluids. In this case we use μPiP to study the bulk mechanical properties of red blood cells. Red blood cell (RBC) deformability is an important parameter in understanding microvascular RBC flow and a loss of RBC deformability can be used as a biomarker for diseases such as malaria, sickle cell disease and diabetes [23-25]. We used dilute RBC solutions from four different mammalian species in order to determine the pressurized deformational flow behavior through the porous medium under μPiP. The flow profiles were then analyzed to develop a dimensional analysis correlation to quantify the deformation of human RBCs.

Initially, horse, bovine, goat, and sheep RBCs were washed and resuspended in 1X PBS solution to reduce the effect of plasma proteins, such as fibrinogen, on RBC aggregation [26]. A pure RBC solution for each animal species was then flowed through a μPiP channel (Whatman grade 4, 2 mm wide, 70 mm long) at a set inlet pressure of 3.85 psig (Fig. 4a). Whatman grade 4 filter paper was used due to its larger pore size (~25 μm) which can accommodate a wide variety of cell sizes. The resulting penetration length of each RBC suspension was measured dynamically as shown, there is approximately 48% decrease in distance covered by horse RBCs as compared to sheep RBCs for the given measured time point (600 sec). Of the four species of RBCs utilized, horse RBCs have the largest average cell diameter, $\langle D \rangle$ followed by bovine, goat and sheep ($\langle D \rangle =$ 4.75±2.13 μm, 4.5±1.93 μm, 4.11±1.87 μm and 3.9±1.87 μm respectively) [27]. As RBC diameter increases, there is a decrease in the observed average RBC suspension velocity as the larger diameter RBCs traverse through the pores within the paper structure. Therefore, the total distance covered by a given RBC suspension after 600 sec is observed to decrease with increasing cell diameter.

The time varying RBC penetration length obtained using this μPiP technique were then correlated with deformation results generated by real time deformability cytometry (RTDC) [27]. RTDC uses high speed camera to capture a change in RBC shape when they flow and deform through thin microfluidic constrictions. The following equation is used to determine cell deformability [28]:

$$d = 1 - \frac{2\sqrt{\pi A}}{P} \qquad (4),$$

where *d* is deformability, and *P* is the deformed cell perimeter, and *A* is the projected cell area. Using RTDC technique, the deformability, *d* of horse, bovine, goat and sheep RBCs were determined as 0.195±0.039, 0.357±0.053, 0.29±0.045 and 0.067±0.027 respectively [27].

We now present a deformation correlation to determine human RBC deformation using μPiP. We develop this model using dimensional analysis. RBCs flow through the paper pores at a velocity proportional to the applied pressure difference across the channel (*ΔP*) and the RBC deformability (*d*). Cells also encounter an opposing a drag force exerted upon their deforming bodies by the paper fiber surfaces as they traverse the pores. Here, we assume this force is proportional to RBC diameter, *D*. Therefore the following scaling argument with unknown scaling constants, *a* and *b* is proposed for the distance covered by bulk RBC flow down the paper channel over time:

$$\frac{\Delta s}{\Delta t} \propto \frac{\Delta P \times d^a}{D^b} \qquad (5),$$

where *a* and *b* are system specific scaling constants that can be experimentally fitted to determine the proportional contribution of deformability and cell size, respectively to the RBC flow. As shown in Fig. 4c, $\frac{\Delta s D^b}{\Delta P d^a}$ vs time (sec) was plotted based on average cell diameter and the known cell deformability values for bovine, goat and sheep blood as measured using RTDC [27]. Values of *a* and *b* were then determined based on the value at which all four datasets maximally collapse into a single universal curve. Shown in Fig. 4c, the value of *b* was determined as 3, which signifies a cell volume type dependence on bulk RBC flow. Similarly, the value of *a* was determined as 0.1, which suggests the influence of deformability itself is small for the bulk RBC flow through paper. This is expected as the pore size of the Whatman grade 4 filter paper (25 μm) is significantly larger than a typical RBC (4-7 μm).

Keeping *a* and *b* constant, this data was then used to determine the unknown deformability for human RBCs (Fig. 5). We first investigated non-deformable RBCs. Human RBCs were crosslinked in 2.5 w/v% glutaraldehyde (glt) and introduced into a pressurized μPiP channel. Glutaraldehyde crosslinks the aminated membrane and interior cytoplasmic proteins and produces a network of polyelectrolytes within the RBC. Chemical treatment produces mechanical stability with minimal influence on RBC diameter and eliminates RBC deformability [29]. As can be seen in figure 5A, glt crosslinked RBCs do not flow through μPiP paper channels even after exposure to a pressure source for 600 seconds. This signifies that RBCs must deform to sucessfully flow through and penetrate the porous paper structure. Next, we flowed non-crosslinked (fresh) human RBCs though the μPiP paper channel. The average diameter of freshly collected human RBCs was determined using brightfield microscopy. Diameters of 50 human RBCs were measured and the average was determined as *D* = 6.35±0.78 μm. To determine the unknown deformability, an average RBC diameter of 6.4 μm was used and from the scaling argument, a deformability value of 0.45 was calculated for human RBC (Fig. 5b). This value is in good agreement with value, d = 0.42 calculated using RTDC [27].

As observed from this example application, the μPiP-based RBC deformation assay leverages pressure driven flow to drive fluid directly and continuously through a porous paper structure. It should be noted that RBC hct was held constant for each RBC experiment and as such was not included as a variable in our dimensional analysis. However, we have observed a weak dependency on sample penetration distance when cell hct varied by more than 5%. If hct is not controlled, it is therefore suggested to include the influence of RBC hct in the dimensional analysis formulation (Eq. 5). The specific paper material properties in μPiP assays offer a new microfluidic variable not typically relevant in paper-based fluidics powered by capillary wicking or with open channel designs. Given the vast availability of different paper materials and pore sizes, the ability to control these variables is a very promising design feature for μPiP and illustrates the benefits for being able to drive flows directly through paper.

3.3 DNA Concentration

The use of μPiP also extends to conventional continuous based microfluidic assays as well. Here, we demonstrate the integration of electrokinetic phenomena into μPiP devices to continuously concentrate DNA electrophoretically. First, a T-shaped channel geometry with two channels - a main flow channel (channel 2) and a secondary DNA concentrate channel (channel 1) – was fabricated (Fig 6a). A copper tape electrode was integrated within the μPiP channel 1 prior to lamination in order to apply an electric field to electrophoretically drive DNA across the channel width and ultimately concentrate the negatively charged biomolecule from a continuous flowing bulk solution in channel 2 and into channel 1 for collection. An 88 bp, randomly generated, double-stranded DNA sequence was used as a model target DNA. The workflow for DNA separation is shown in Fig. 6b. A buffer solution containing 50 nM DNA was flowed continuously into channel 2 at flow rate of 5 μL/min. A 100V DC voltage was simultaneously applied across the electrodes to create a transverse electric field within the channel to electrophoretically deflect the DNA target across the main channel and into channel 1.

After running the electrophoresis operation for 20 minutes, outlet paper samples were cut and collected from both the DNA-enriched (channel 1) and DNA-depleted channel (channel 2). DNA from paper was then eluted in diH_2O and qPCR was used to evaluate DNA concentration. This process was performed with a voltage of 100 V applied to the electrode in channel 1 and channel 2 grounded and without an applied voltage. To visualize DNA deflection after the experiment, a ChemiDoc MP gel imaging system (Bio-Rad Laboratories, Inc) was used to observe the DNA-based fluorescence intensity in the paper device. As mentioned earlier, SYBR binds with DNA, resulting in a SYBR-DNA complex which is excited at 497 nm. Fig 6c shows the resulting fluorescence image, where DNA has been deflected into channel 1, corresponding to fluorescence increase in the channel 1 collection zone. Finally, DNA concentration was quantified by qPCR. As depicted in Fig. 6d, qPCR analysis shows a 30-fold increase in DNA concentration as compared to the initial non-concentrated stock solution. This increase in concentration was achieved using a relatively low 100V DC voltage, which can be readily adapted for use in a portable format for enhancing sensitivity of PCR assays. The μPiP workflow offers the benefits of continuous flow microfluidics with a significant reduction in fabrication workflow complexity and device assembly time. Further, unlike traditional open channel designs, a portion of the paper channel itself can be physically cut from the device to readily access concentrated sample. We therefore believe that DNA concentration by μPiP is a low-cost and useful alternative to open channel microfluidics.

4. Conclusions

In conclusion, we have demonstrated a microfluidic fabrication technique for producing laminated paper microchannels. Devices fabricated using the μPiP technique can be controllably pressurized for use in active fluid flow control. A mathematical transport model based on capillary and pressure driven flow was developed and shown to accurately describe the μPiP flow behavior. We demonstrated the use of μPiP in reproducing “classical” microfluidic flows and also with more advanced microfluidic tasks. In particular, we presented the use of the μPiP technique to characterize RBC mechanical deformability. In addition, we demonstrated the integration of electrokinetics into μPiP by electrophoretically concentrating DNA from a bulk solution. Unlike open channel microfluidics, biomolecules such as DNA can be concentrated at a particular μPiP channel and can be instantly accessed by cutting out that channel. In addition, analytes can be lyophilized and stored in paper channels. A variety of microfluidic designs and complex fluids can be utilized using this method, and the fabrication workflow will enable researchers to quickly design, build, test, and share device designs with minimal effort. Further, because small portable laser cutters and tesla coils can be used for device fabrication, it is feasible to design μPiP devices at a central location then share, fabricate and deploy these devices "on-demand" in distant remote areas such as war zones, outer space or in rural low-resource settings. This fabrication technique is also scalable; the μPiP fabrication workflow can be used to commercially produce thousands of devices per day with minimal capital investment. Future work will demonstrate that other features of traditional microfluidics, including valves, and sensors, that can also be integrated into PDMS-paper structure for μPiP-based electrochemical and electrokinetic analysis. We therefore expect that μPiP will be beneficial for both academia and industry and serve as a powerful method to potentially bridge the translation and product development gap between rapid device prototyping in academia and that of industrial scale microfluidic manufacturing and serve as a low-cost minimal barrier of entry for researchers interested in microfluidics. With further development, our novel fabrication technique has the potential to democratize microfluidic innovation by significantly reducing fabrication costs and enabling the manufacturing of robust microfluidic devices at scale using a workflow that any researcher, regardless of funding, can successfully utilize.

Acknowledgements

The PI gratefully acknowledges support from a NASA Early Career Faculty award (80NSSC19K1401).

References

1. Convery, N. and N. Gadegaard, *30 years of microfluidics.* Micro and Nano Engineering, 2019. **2**: p. 76-91.
2. Faustino, V., et al., *Biomedical microfluidic devices by using low-cost fabrication techniques: A review.* J Biomech, 2016. **49**(11): p. 2280-2292.
3. Walsh, D.I., 3rd, et al., *Enabling Microfluidics: from Clean Rooms to Makerspaces.* Trends Biotechnol, 2017. **35**(5): p. 383-392.
4. *Microfluidics Market Size, Share & Trends Analysis Report By Application (Lab-on-a-Chip, Organs-on-Chips, Continuous Flow), By Technology (Medical, Non-*

Medical), By Material, And Segment Forecasts, 2020 - 2027. 2020, Grand View Research.

5. Gale, B., et al., *A Review of Current Methods in Microfluidic Device Fabrication and Future Commercialization Prospects.* Inventions, 2018. **3**(3).
6. Carrell, C., et al., *Beyond the lateral flow assay: A review of paper-based microfluidics.* Microelectronic Engineering, 2019. **206**: p. 45-54.
7. Martinez, A.W., et al., *Patterned paper as a platform for inexpensive, low-volume, portable bioassays.* Angew Chem Int Ed Engl, 2007. **46**(8): p. 1318-20.
8. Sher, M., et al., *Paper-based analytical devices for clinical diagnosis: recent advances in the fabrication techniques and sensing mechanisms.* Expert Rev Mol Diagn, 2017. **17**(4): p. 351-366.
9. Soum, V., et al., *Programmable Paper-Based Microfluidic Devices for Biomarker Detections.* Micromachines (Basel), 2019. **10**(8).
10. Osborn, J.L., et al., *Microfluidics without pumps: reinventing the T-sensor and H-filter in paper networks.* Lab Chip, 2010. **10**(20): p. 2659-65.
11. Määttänen, A., et al., *Paper-based planar reaction arrays for printed diagnostics.* Sensors and Actuators B: Chemical, 2011. **160**(1): p. 1404-1412.
12. Islam, M.N., et al., *Developing Paper Based Diagnostic Technique to Detect Uric Acid in Urine.* Front Chem, 2018. **6**: p. 496.
13. Andres W. Martinez, S.T.P., Emanuel Carrilho, and George M. Whitesides, *Diagnostics for the Developing World: Microfluidic Paper-Based Analytical Devices.* Analytical Chemistry, 2010(82): p. 3-10.
14. Cheng, C.M., et al., *Paper-based ELISA.* Angew Chem Int Ed Engl, 2010. **49**(28): p. 4771-4.
15. Jokerst, J.C., et al., *Development of a paper-based analytical device for colorimetric detection of select foodborne pathogens.* Anal Chem, 2012. **84**(6): p. 2900-7.
16. Glavan, A.C., et al., *Rapid fabrication of pressure-driven open-channel microfluidic devices in omniphobic R(F) paper.* Lab Chip, 2013. **13**(15): p. 2922-30.
17. Yi, X., et al., *A simple method of fabricating mask-free microfluidic devices for biological analysis.* Biomicrofluidics, 2010. **4**(3).
18. Shin, J.-H., et al., *A stand-alone pressure-driven 3D microfluidic chemical sensing analytic device.* Sensors and Actuators B: Chemical, 2016. **230**: p. 380-387.
19. Mavrogiannis, N., et al., *Microfluidics made easy: A robust low-cost constant pressure flow controller for engineers and cell biologists.* Biomicrofluidics, 2016. **10**(3): p. 034107.
20. Liu, Z., et al., *Experimental and numerical studies on liquid wicking into filter papers for paper-based diagnostics.* Applied Thermal Engineering, 2015. **88**: p. 280-287.
21. MacDonald, B.D., *Flow of liquids through paper.* Journal of Fluid Mechanics, 2018. **852**: p. 1-4.
22. Mai, V.-P., C.-H. Ku, and R.-J. Yang, *Porosity estimation using electric current measurements for paper-based microfluidics.* Microfluidics and Nanofluidics, 2019. **23**(4).

23. Passos, A., et al., *The effect of deformability on the microscale flow behavior of red blood cell suspensions.* Physics of Fluids, 2019. **31**(9).
24. Faustino, V., et al., *A Microfluidic Deformability Assessment of Pathological Red Blood Cells Flowing in a Hyperbolic Converging Microchannel.* Micromachines (Basel), 2019. **10**(10).
25. Huisjes, R., et al., *Squeezing for Life - Properties of Red Blood Cell Deformability.* Front Physiol, 2018. **9**: p. 656.
26. Brust, M., et al., *The plasma protein fibrinogen stabilizes clusters of red blood cells in microcapillary flows.* Sci Rep, 2014. **4**: p. 4348.
27. Crivellari, F., *Microfluidics & AC Electrokinetics: Developing Biosensors for Portable Diagnostics and Autologous Blood Doping in Endurance Athletes*, in *Chemical Engineering*. 2018, John Hopkins University: John Hopkins Sheridan Libraries.
28. Panhwar, M.H., et al., *High-throughput cell and spheroid mechanics in virtual fluidic channels.* Nat Commun, 2020. **11**(1): p. 2190.
29. Gordon, J.E., Z. Gagnon, and H.-C. Chang, *Dielectrophoretic discrimination of bovine red blood cell starvation age by buffer selection and membrane cross-linking.* Biomicrofluidics, 2007. **1**(4): p. 044102.

Figures

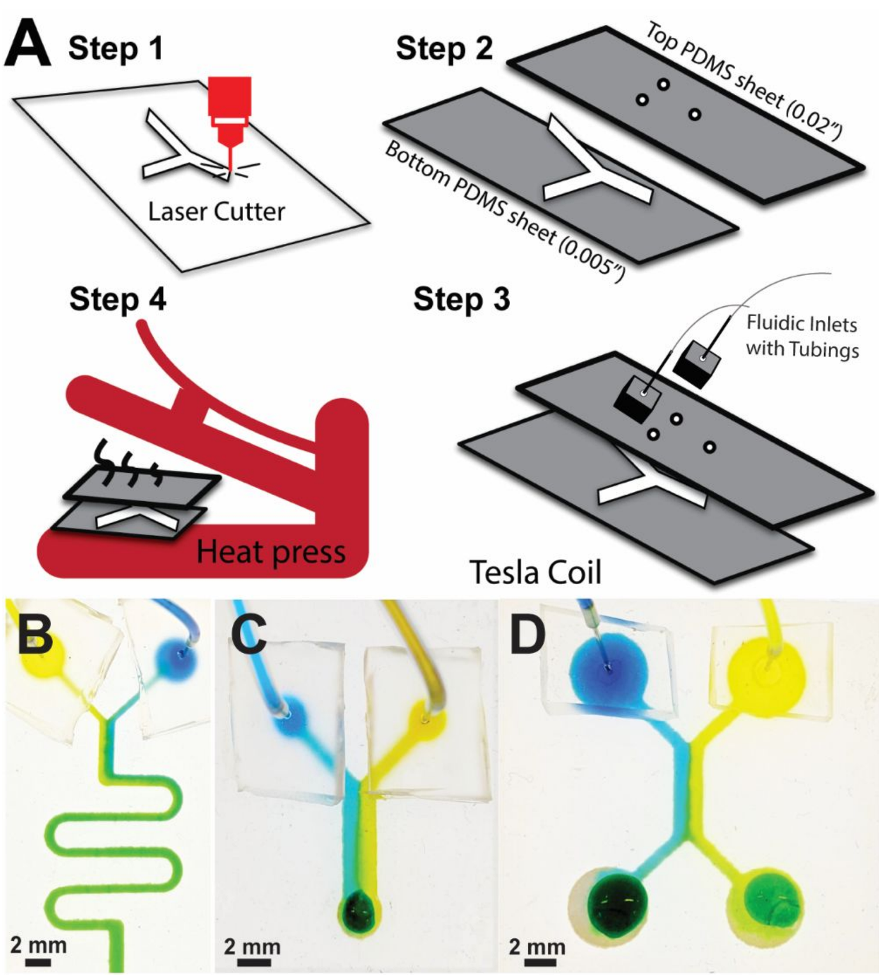
A
Step 1
Laser Cutter
Step 2
Top PDMS sheet (0.02")
Bottom PDMS sheet (0.005")
Step 4
Heat press
Step 3
Fluidic Inlets
with Tubings
Tesla Coil
B
C
D
2 mm
2 mm
2 mm

Figure 1. Microfluidic pressure in paper (μPiP) for rapidly fabricating continuous flow paper-based devices. (a) Fabrication workflow. (b) Serpentine mixer. (c) Y-channel geometry. (d) H-channel geometry**.**

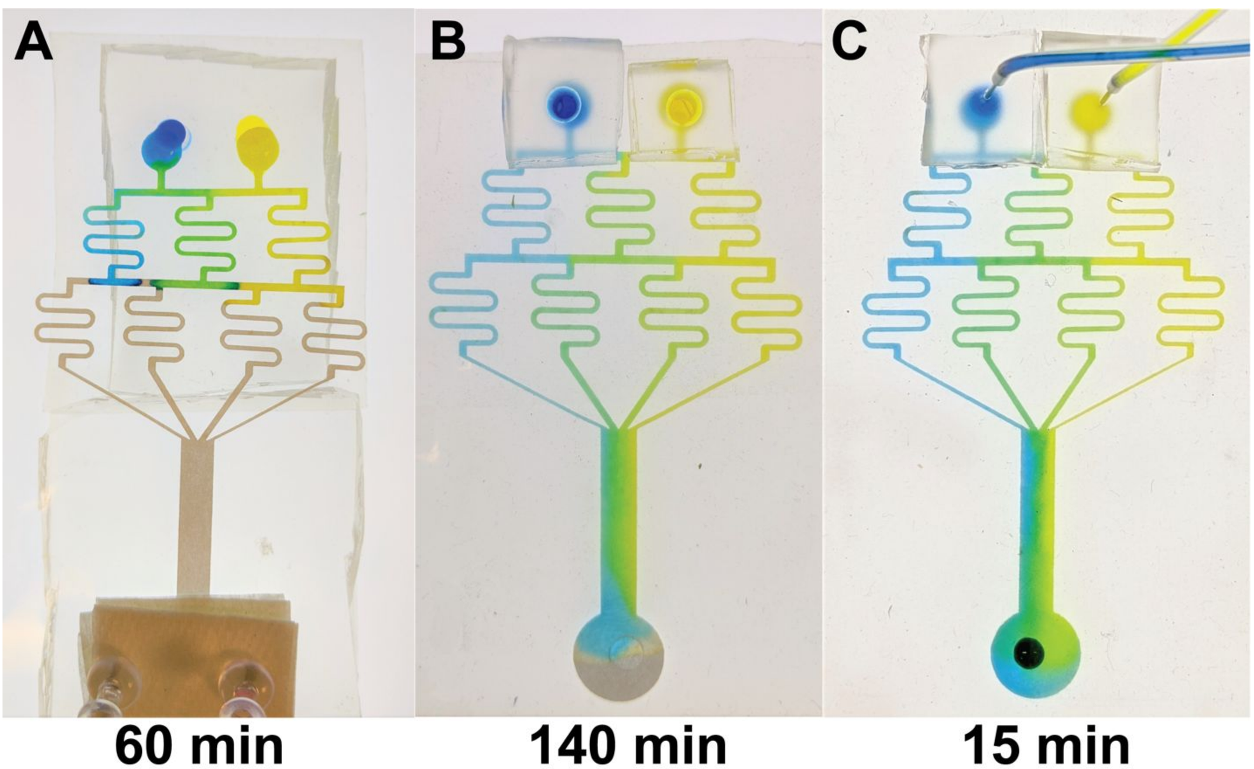

Figure 2. Comparison of classical "Christmas Tree" gradient generator. (a) Non-laminated passive wicking device fails to fully wet due to evaporation. (b) Lamination allows for full priming by wicking in 140 min. (c) Laminated μPiP channels fully prime in 15 mins and continue operating continuously.

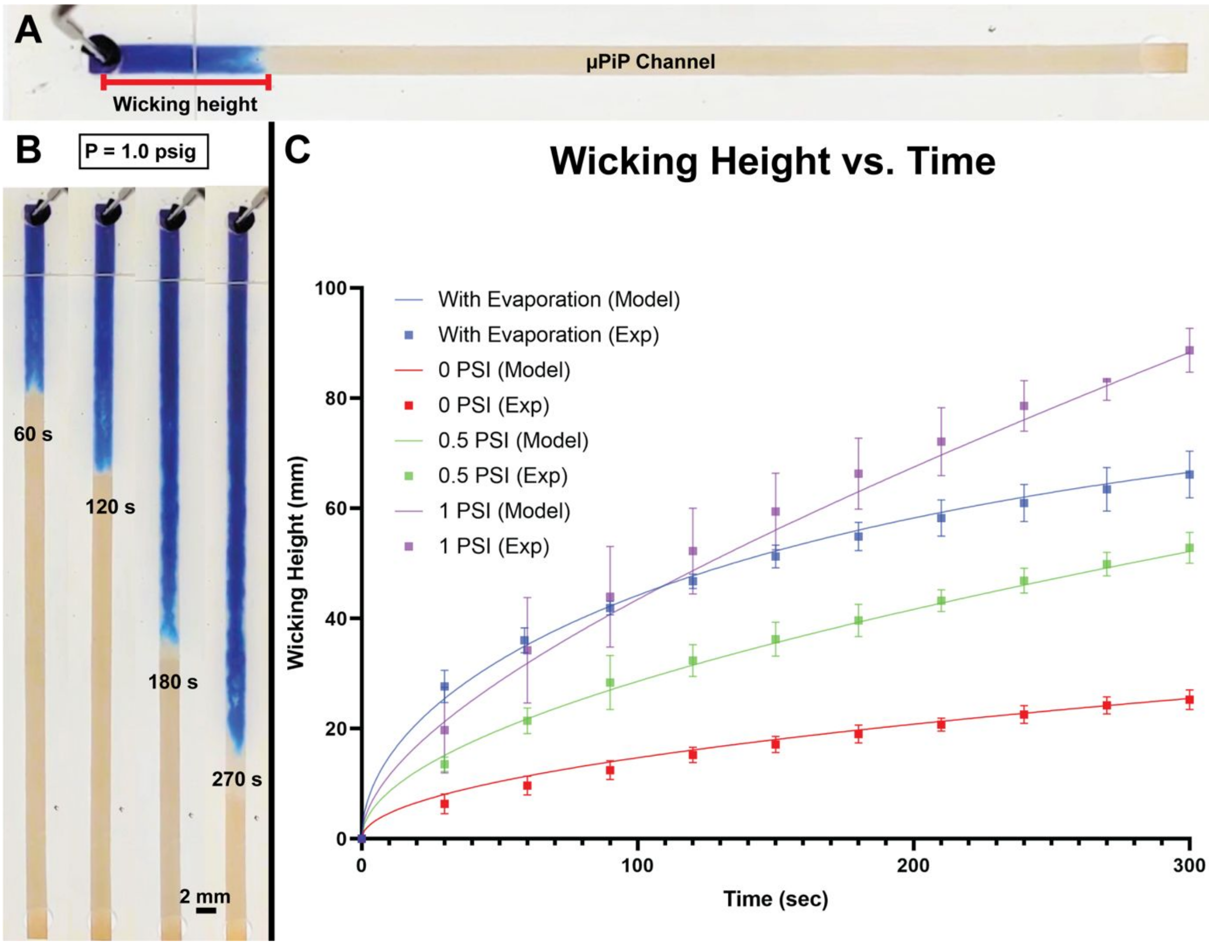

Figure. 3 Experimental wicking height as a function of time down a µPiP channel. (a) Fluid flow observed as a penetrating wicking height. (b) Wicking height of colored deionized water in response to an external pressure at different time points. (c) Comparison of experimental wicking height with the mathematical model for capillary driven flow with evaporation (blue), capillary flow for compressed paper (red), capillary and pressure driven flow at different applied pressure (green and purple).

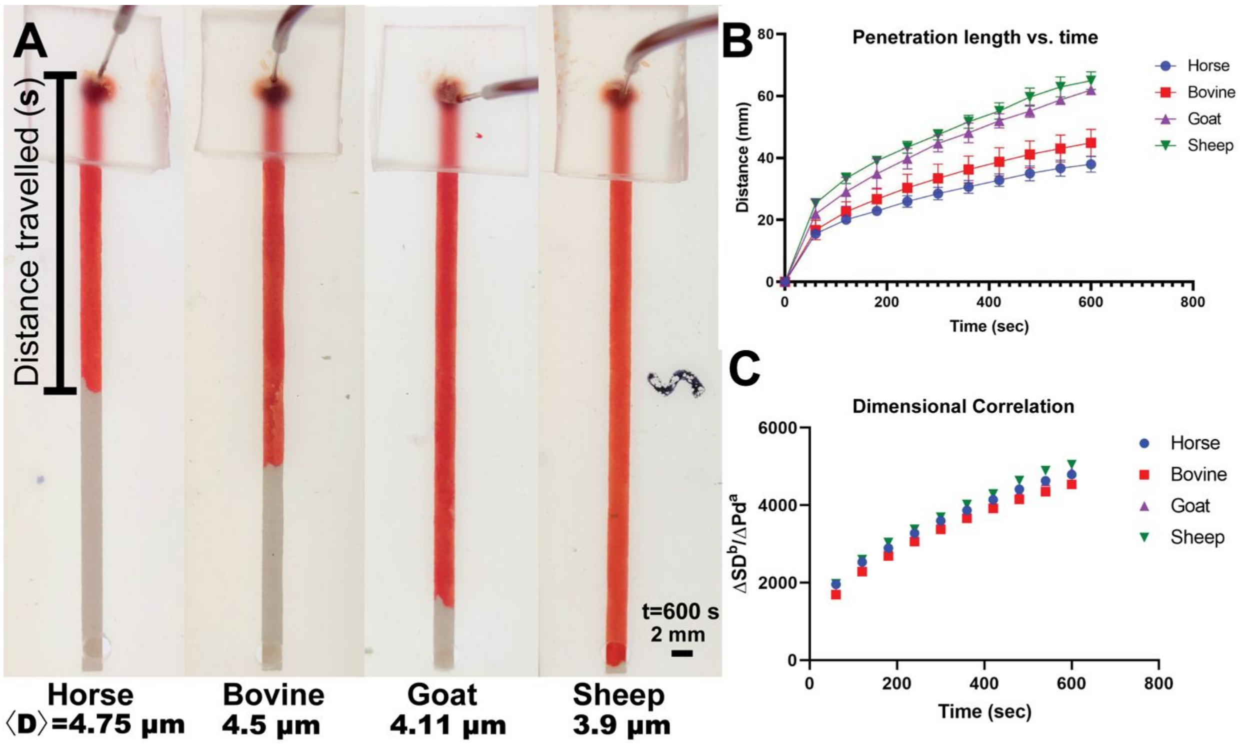

Figure 4. µPiP flow of animal RBCs for deformability analysis. (a) RBC penetration distance, s of horse, bovine, goat and sheep RBCs at a penetration time, t=600 s. (b) RBC penetration distance versus time. Distance traveled increases with decreasing RBC average diameter,$\langle D \rangle$. (c) Scaled dimensional correlation of penetration profiles of animal RBCs.

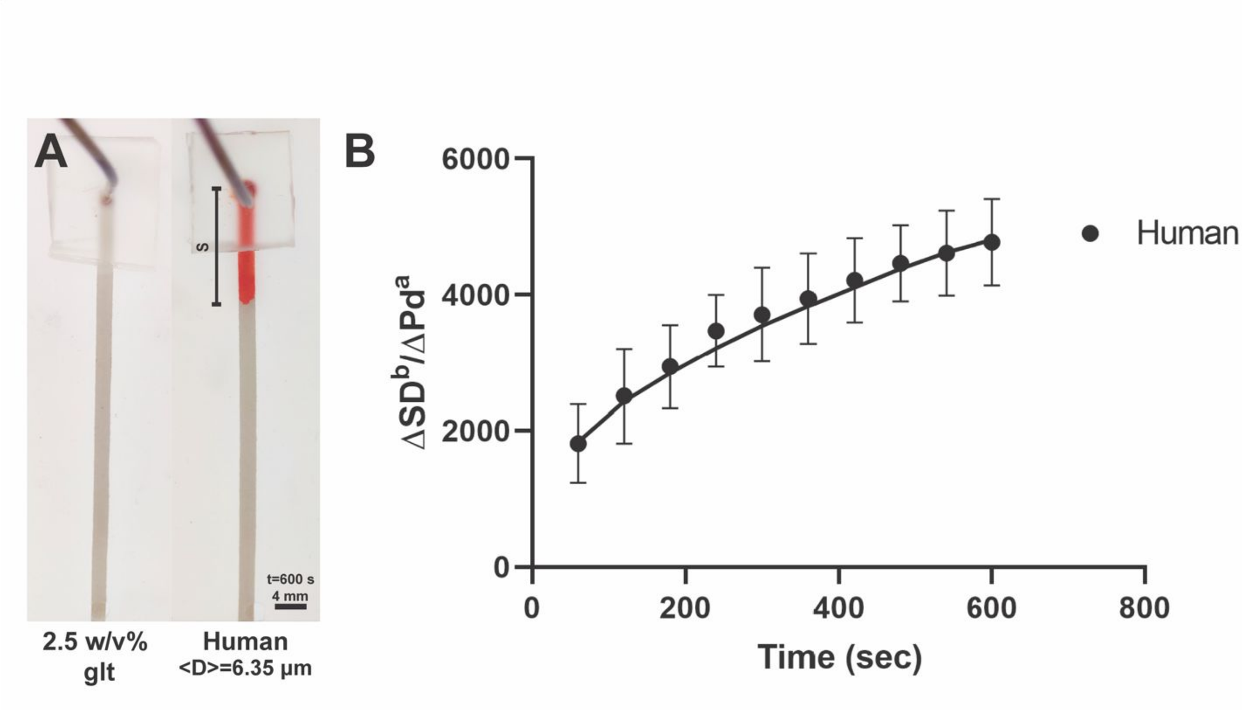

Figure 5. (a) µPiP flow of human RBCs without and with 2.5 w/v% glutaraldehyde crosslinking (average diameter, $\langle D\rangle = 6.35\ \mu m$) after 600 s. (b) Scaled penetration profile versus time fitted to deduce unknown RBC deformability.

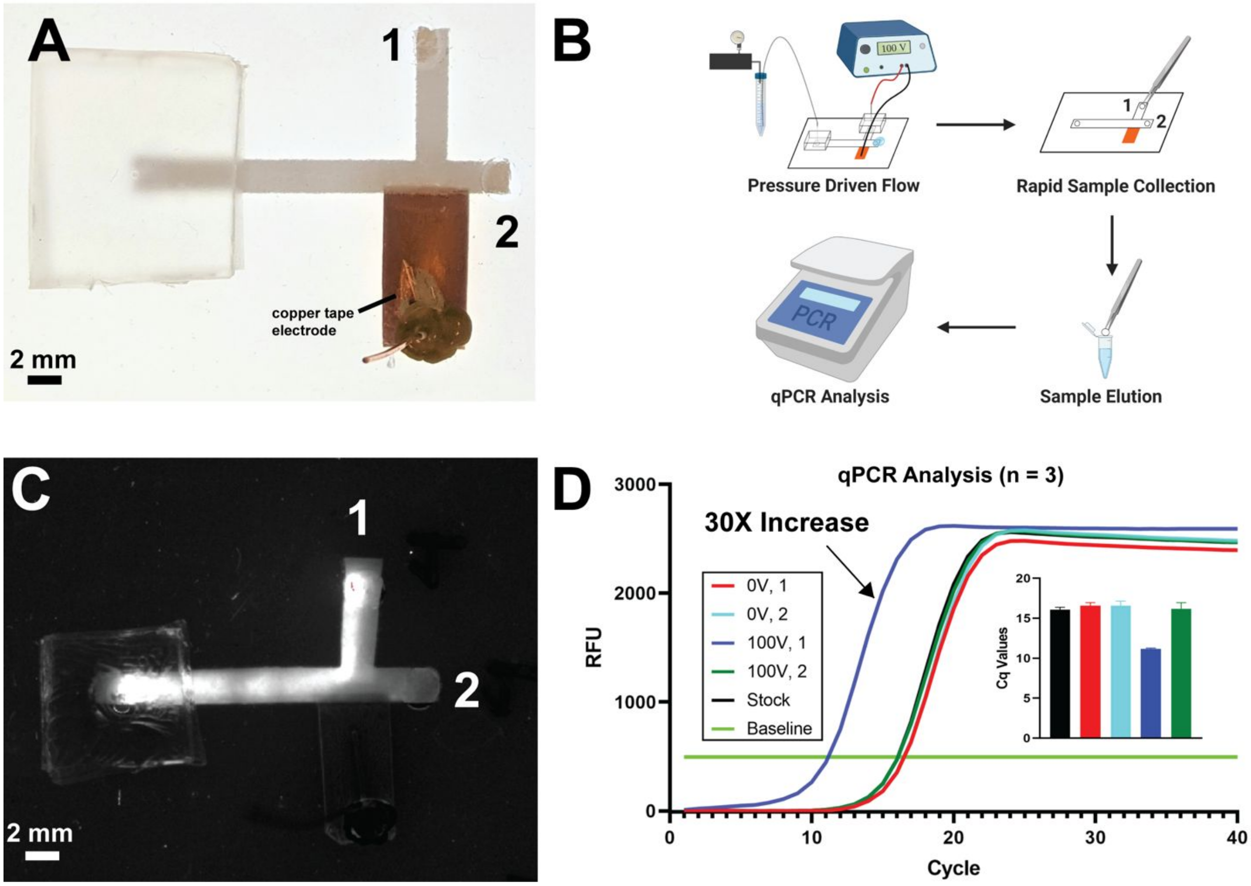

Figure 6. Continuous electrophoresis concentration of DNA in paper. (a) μPiP device with a main channel, 2 and a concentration channel, 1. A conductive copper tape electrode provides a DC electric field for inducing electrophoresis. (b) DNA concentration workflow. (c) Fluorescently tagged DNA imaged using a Bio-Rad gel imager illustrates path of electrophoretically concentrated DNA. (d) qPCR curves demonstrate a 30X increase in DNA concentration by μPiP electrophoresis.